LAWRENCE
LIVERMORE
NATIONAL
LABORATORY

UCRL-CONF-208296

Design of a Multi-Channel Ultra-High Resolution Superconducting Gamma-Ray Spectrometer

S. Friedrich, S. F. Terracol, T. Miyazaki, O. B. Drury, Z. A. Ali, M. F. Cunningham, T. R. Niedermayr, T. W. Barbee Jr., J. D. Batteux, S. E. Labov

December 1, 2004

SPIE (The International Society for Optical Engineering) 49th Annual Meeting 2004
Denver, CO, United States
August 2, 2004 through August 6, 2004

Disclaimer

Invited Paper

Design of a Multi-Channel Ultra-High Resolution Superconducting Gamma-Ray Spectrometer

Stephan Friedrich*, Stephane F. Terracol, Toshiyuki Miyazaki, Owen B. Drury, Zaheer A. Ali, Mark F. Cunningham, Thomas R. Niedermayr, Troy W. Barbee Jr., Jan D. Batteux, Simon E. Labov

Advanced Detector Group, Lawrence Livermore National Laboratory, L-270, Livermore, CA 94550

ABSTRACT

Superconducting Gamma-ray microcalorimeters operated at temperatures around ~0.1 K offer an order of magnitude improvement in energy resolution over conventional high-purity Germanium spectrometers. The calorimeters consist of a ~1 mm^3 superconducting or insulating absorber and a sensitive thermistor, which are weakly coupled to a cold bath. Gamma-ray capture increases the absorber temperature in proportion to the Gamma-ray energy, this is measured by the thermistor, and both subsequently cool back down to the base temperature through the weak link. We are developing ultra-high-resolution Gamma-ray spectrometers based on Sn absorbers and superconducting Mo/Cu multilayer thermistors for nuclear non-proliferation applications. They have achieved an energy resolution between 60 and 90 eV for Gamma-rays up to 100 keV. We also build two-stage adiabatic demagnetization refrigerators for user-friendly detector operation at 0.1 K. We present recent results on the performance of single pixel Gamma-ray spectrometers, and discuss the design of a large detector array for increased sensitivity.

Keywords: Microcalorimeters, Mo/Cu multilayers, detector arrays, Gamma spectroscopy, nuclear non-proliferation

1. INTRODUCTION

1.1. Operating principle

Cryogenic Gamma-ray microcalorimeters operated at temperatures of ~0.1 K offer an order of magnitude improvement in energy resolution over conventional high-purity germanium (HPGe) detectors. They have been developed over the last decade for applications ranging from nuclear analysis to high-energy astrophysics [1]. Microcalorimetry can significantly enhance the analysis of complicated nuclear mixtures when HPGe detectors cannot separate the individual Gamma emission lines from different isotopes. It also enables precise measurements of Doppler broadening for dynamic studies in nuclear astrophysics, or of Lamb shifts for tests of the Standard Model.

Cryogenic Gamma-ray calorimeters typically consist of a bulk absorber with heat capacity C attached to a sensitive thermistor, both of which are weakly coupled to a cold bath through a thermal conductance G. In the simplest case [2], random energy fluctuations $4k_BT^2G$ across this thermal conductance fundamentally limit the energy resolution of microcalorimeters to

$$\Delta E_{FWHM} \approx 2.355\sqrt{k_BT^2C} \qquad (1)$$

Intuitively, equation (1) can be understood considering that the energy in the absorber is mostly stored in phonon lattice vibrations. At a temperature T, the average phonon carries ~k_BT of energy, and the absorber stores a total energy of ~CT. The total number of phonons is thus given by ~$CT/k_BT = C/k_B$. Assuming Poisson's statistics, this number of phonons will fluctuate by $\sqrt{(C/k_B)}$, thereby leading to rms energy fluctuations of $k_BT\sqrt{(C/k_B)} = \sqrt{(k_BT^2C)}$. A more rigorous derivation of the energy fluctuations from the derivatives of the partition function in the grand canonical ensemble shows that equation (1) is in fact correct for arbitrary weakly coupled systems at temperature T. Since average excitation energies at ~0.1 K are only of order ~10 μeV per phonon, statistical fluctuation in the number of phonons impose a much lower limit on the energy resolution of calorimeters compared to conventional Gamma spectrometers where excitation energy per electron hole pair are of order ~1eV.

Corresponding author: friedrich1@llnl.gov; +1 (925) 423-1527 (phone), +1 (925) 424-5512 (fax)

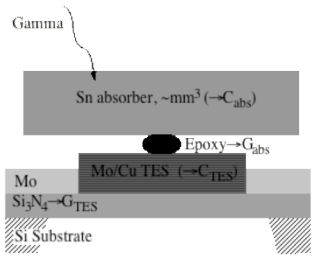

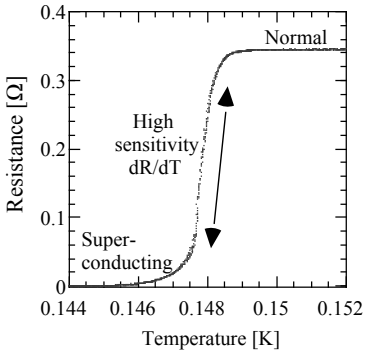

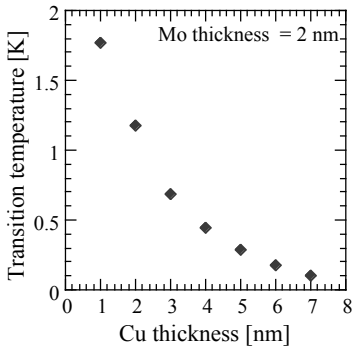

Fig.1. (left) Schematic design of a microcalorimeter (not to scale). Fig.2. (center) Superconducting-to-normal transition in a Mo/Cu multilayer TES calorimeter. The steep transition ensures high sensitivity. Fig. 3. (right) Adjustability of the superconducting transition temperature as a function of the Mo:Cu ratio. The Mo thickness is 2 nm for all devices in this test series.

High energy resolution single photon Gamma-ray calorimeters thus require low temperatures T and low heat capacity C. Operating temperatures around ~0.1 K are a practical compromise, since they are comparably easy to attain with modern adiabatic demagnetization or dilution refrigerators. The maximum absorber size is then set by the heat capacity of the absorber material and the desired energy resolution. In addition, the heat capacity sets the detector's count rate capabilities, since the return of the detector to the bath temperature T_{bath} takes a characteristic relaxation time $\tau = C/G$. Superconducting, insulating or semi-metallic absorbers are preferred, because they do not have an electronic contribution to the specific heat. For typical absorber materials such as Sn, HgTe or Bi, a desired energy resolution below 100 eV limits the absorber volume to ~1 mm^3 for a single pixel detector. Larger spectrometers for higher sensitivity (in nuclear analysis) or for imaging (in astrophysics) require the fabrication of detector arrays. In addition, multi-pixel arrays also increase the total count rate capabilities by a factor equal to the number of independent pixels.

1.2. Current state of the art

Several thermistor technologies are currently being developed as sensors for cryogenic Gamma-ray or hard X-ray detectors. Microcalorimeters based on ion-implanted Si, originally developed for X-ray astrophysics [2, 3], have been modified to allow precise measurements of Lamb shifts in hard X-ray emission lines of highly-charged ions as a precise test of the Standard Model of particle physics [4]. Neutron transmutation doped (NTD) Ge detectors have been developed for and used in laboratory astrophysics [5], and a balloon-borne mission to study ^{44}Ti nuclear emission lines from supernova remnants is currently being planned [6]. These sensors all use bulk absorbers of different size and composition glued to a cryogenic thermistor, and have achieved an energy resolution between ~50 and ~100 eV FWHM for energies below 122 keV. More recently, magnetic microcalorimeters based on Er-doped Au sensors, in which the increase in temperature is detected as a change in sensor magnetization, have emerged as an alternative cryogenic sensor for hard X-ray and Gamma-ray detection, with an energy resolution currently of 130 eV FWHM at 122 keV [7].

We are developing Gamma-ray spectrometers based on superconducting-to-normal transition edge sensors (TESs) for nuclear non-proliferation applications [8, 9]. They consist of a superconducting Mo/Cu multilayer film held at the transition between its superconducting and its normal state where its resistance varies sensitively with temperature. A bulk Sn absorber is attached for increased efficiency (figure 1 and 2). The Mo/Cu TES is held on a thin SiN membrane that provides the weak thermal link to the cold bath. The thickness of the superconducting Mo (T_c(Mo) ≈ 1 K) and the normal metal Cu films is chosen to produce the desired intermediate transition temperature through the proximity effect (figure 3). Since the TES resistance is low (cf. figure 2), a superconducting quantum interference device (SQUID) is used as a preamplifier. Our detectors have achieved an energy resolution of ~60 eV at 60 keV, about a factor of 5 better than the Fano limit for conventional HPGe detectors at that energy [10]. We also develop frequency-based multiplexing technology to read out multiple Gamma-detector pixels with a single SQUID preamplifier [10]. This can be done without degradation of detector resolution, and is crucial for the readout of large arrays to limit the heat load into the cold stage due to the number of wires. In addition, we have built several two-stage adiabatic demagnetization refrigerators for comparably user-friendly detector operation at ~0.1 K [11]. Here we discuss the current performance of the spectrometers, as well as the design of a multi-channel spectrometer for increased sensitivity.

2. THEORY

2.1. Detector design and SPICE modeling

Simple transition edge sensor (TES) microcalorimeters, i.e. those where absorber and thermistor are either identical or are sufficiently well coupled to be considered a single thermal unit, have been under development for high-resolution single photon spectroscopy below ~10 keV for over a decade [1]. For optical or soft X-ray detection, they consist of a bilayer TES that simultaneously serves as the photon absorber. For energies between ~1 keV and ~10 keV, a thin film absorber is usually deposited in direct electrical and thermal contact with the TES. Fast thermalization and thermal stability considerations require the impedance R_{TES} of a simple TES microcalorimeter to be low, typically on the order ~0.1 Ω [12]. This precludes a direct FET-based readout, in favor of superconducting quantum interference device (SQUID) preamplifiers (figure 4). The TES is typically voltage biased across a shunt resistor $R_S << R_{TES}$ to benefit from electrothermal feedback (ETF), i.e. the reduction in bias power V_{bias}^2/R_{TES} whenever photon absorption increases the temperature and thus the resistance of the TES. ETF maintains the detector bias constant at a resistance $R_{TES}(T)$ where the bias power V_{bias}^2/R_{TES} balances the power flow into the substrate $(T-T_{bath})G_{TES}$, it speeds up the pulse decay by reducing the bias power during a pulse when R_{TES} is increased, and it suppresses the phonon noise of the TES by counteracting random TES temperature fluctuations [13]. TES microcalorimeters with ETF can theoretically achieve an energy resolution of order ~1eV FWHM, and several groups have attained an energy resolution of ~4 to ~6 eV FWHM at 6 keV, with pulse decay times on the order of ~100 μs [14-17].

Composite microcalorimeters consisting of a small TES thermistor and a large attached bulk absorber allow increasing the absorption efficiency and thus the spectrometer sensitivity above ~10 keV while minimizing the associated increase in noise. Still, there are now two finite thermal conductances, one from the glue between the bulk absorber and the TES (G_{abs}), and one from the membrane between the TES and the cold bath (G_{TES}), and both contribute energy fluctuations k_BT^2G to the total noise (cf. figure 1). In addition, the phonon noise $k_BT^2G_{abs}$ from the finite conductance between the absorber and the TES is no longer suppressed by the electrothermal feedback, which only acts on the TES itself and does not counteract the random energy fluctuations between TES and absorber. On the other hand, the finite conductance serves as a thermal bottleneck and thereby reduces spatial variation in the detector response. Other noise sources, such as the current noise of the SQUID preamplifier or the Johnson noise of the resistive components of the circuit, can be kept sufficiently low to not further degrade the energy resolution.

To simulate the response of a composite microcalorimeter in a particular circuit configuration, and to optimize its design for best energy resolution, we can exploit the analogy between thermal and electric circuits. Identifying temperatures with voltages, power flow with currents, heat capacities with capacitances and thermal with electrical conductances ($G \equiv 1/R$), we can integrate thermal and electrical circuits and calculate the response using the whole range of commercially available SPICE circuit simulation routines [18, 19]. The implementation of such a simulation is shown in figure 5. The left part of the simulation represents the composite microcalorimeter, characterized by the heat capacities of the absorber (C_{abs}) and TES microcalorimeter (C_{TES}), and by the two thermal conductances G_{abs} and G_{TES}.

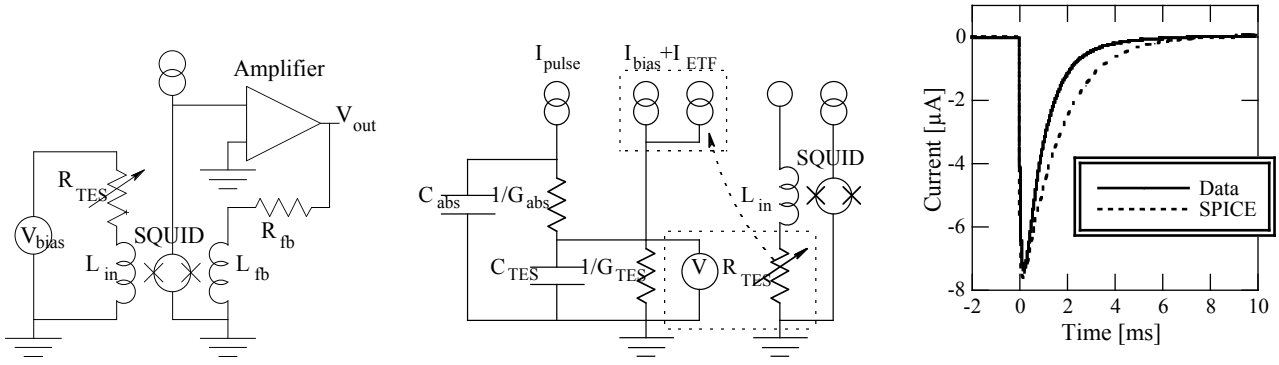

Fig. 4. (left) Schematic of the electronic readout for a cryogenic microcalorimeter. The voltage bias is implement through a shunt resistor $R_S << R_{TES}$ in parallel with R_{TES} and L_{in}. Fig. 5. (center) SPICE model of a composite microcalorimeter (feedback electronics not shown). Fig. 6. (right) Simulated current of the SPICE model (dotted), compared to measured 60 keV Gamma-ray pulse (solid).

The calorimeter is coupled to the electronic readout through the resistance of the TES, represented as a dotted rectangle in figure 5. The temperature dependence of the TES resistance is parameterized by the dimensionless sensitivity $\alpha \equiv T/R_{TES}\partial R_{TES}/\partial T$. The TES bias is represented as a current into the TES, and the absorption of a Gamma ray corresponds to a δ-function current input into the absorber. Electrothermal feedback is implemented as a change in TES bias controlled by a change in TES resistance (dotted line). The SPICE simulation reproduces the measured current waveform reasonably well (figure 6). The comparison with measured pulse shapes also permits extracting certain device parameters that are difficult to predict from known material constants, such as the thermal conductance of the epoxy dot between the absorber and the TES.

We can now simulate the performance of the composite microcalorimeters for a range of different device parameters. Figure 7 shows the different contributions to device noise. For most of the signal band of a few kHz the noise is dominated by the phonon noise G_{abs} between absorber and TES. Only at low frequencies below $G_{abs}/2\pi C_{abs}$ this noise contribution is reduced, because the absorber cannot change its temperature relative to TES and can thus benefit from electrothermal feedback (ETF). Increasing G_{abs} therefore improves the device performance, since it increases the frequency range over which ETF reduces the dominant noise source. The Johnson noise contribution $4k_BT/R_{TES}$ only contributes at very high frequencies and is negligible. The theoretical energy resolution for any set of detector parameters can be calculated from the simulated spectral noise density by integration over the appropriate optimum filter bandwidth (figure 8) [2]. As expected from equation (1), the noise for composite microcalorimeters increases with increasing absorber heat capacity and thus absorber volume. The detector resolution improves with increasing thermal coupling G_{abs} between absorber and TES, with typical values for G_{abs} in the 10 nW/K range for the ~200 µm diameter ~25 µm thick epoxy dots used in our detector design.

One therefore faces a trade-off between energy resolution and absorption efficiency, with the overall performance improving with increasing G_{abs}. For many ultra-high resolution nuclear analyses an energy resolution below 100 eV is desirable, and we typically choose an absorber volume to achieve this given the constraint of $G_{abs} \approx$ 10 nW/K. We are currently investigating alternative adhesives to increase G_{abs}. It is surprising that most cryogenic Gamma spectrometers to date rely on Sn absorbers [4, 5, 9], although e.g. Ta has higher absorption efficiency and lower heat capacity. The reasons for poor resolution of calorimeters with Ta and other high-Z absorbers are not understood, and will be the subject of future studies.

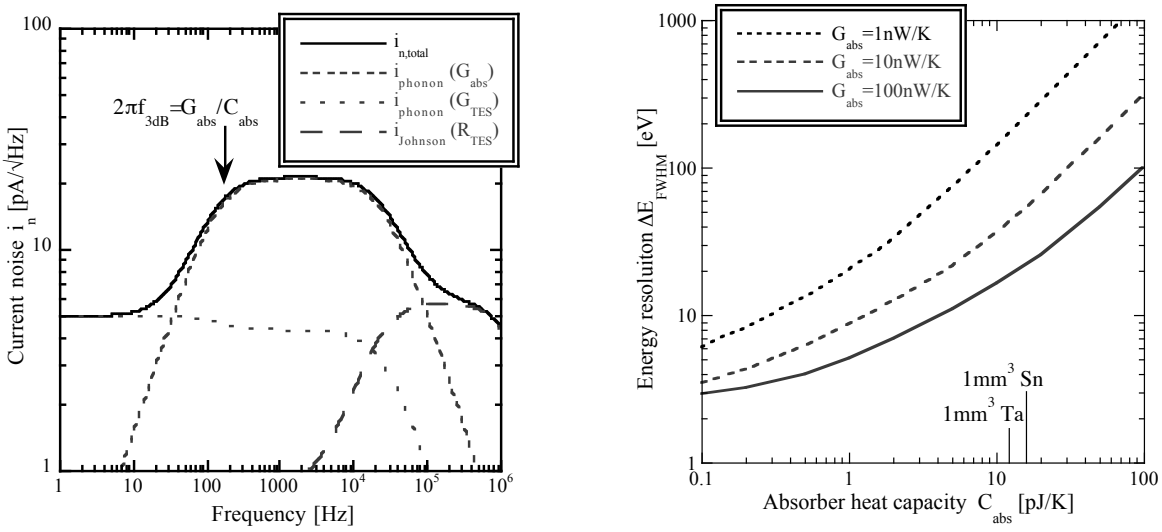

Fig. 7. (left) SPICE simulation of the different noise contributions for a typical Gamma ray detector (C_{abs} = 10 pJ/K, C_{TES} = 1pJ/K, G_{abs} = 10 nW/K, G_{TES} = 1 nW/K, α =100, T = 0.1 K). Electrothermal feedback suppresses the phonon noise only at frequencies below $G_{abs}/2\pi C_{abs}$ where absorber and TES are thermally coupled. Fig. 8. (right) Simulated energy resolution of a TES Gamma-ray calorimeter as a function of absorber heat capacity, i.e. of absorber size and thus efficiency. The numerical values of the heat capacities for 1 mm^3 of two absorber materials (Sn and Ta) at 0.1 K are marked for comparison.

3. EXPERIMENT

3.1. Detector fabrication

The Mo/Cu multilayer TESs are fabricated by photolithography on SiN membranes on Si using a 4" full wafer process. The p-type Si wafers are ~500 to ~600 μm thick, cut in <100> orientation, and are commercially available from WaferNet Inc. A 500 nm SiN layer with a tensile stress of 785 MPa is grown thermally grown on both sides of the wafer. To define the SiN membranes, square windows are etched in the SiN on the back side of the wafer using a 90% CF_4 10% O_2 plasma etch, followed by a 44% KOH etch at 65 ˚C to remove the bulk Si and produce a pattern of free-standing thin SiN membranes between 1.25 mm × 1.25 mm and 2.25 mm × 2.25 mm. The Mo/Cu multilayers are sputter-deposited in a chamber designed for X-ray multilayer optics. Fifteen Mo/Cu bilayers, each consisting of 4 nm of Mo and 9 nm of Cu, and a 9 nm Cu capping layer, are sputter-deposited at a pressure 1 mTorr by rotating the wafer inside the chamber over a Mo and a Cu sputtering gun. The rotation speed and the sputtering power set the layer thickness, and ensure uniform coverage in direction of the wafer rotation, although there is a small gradient in perpendicular direction over some part wafer since typical x-ray multilayer optics are smaller than 4". The resulting 204 nm multilayer has an rms roughness of ~1 nm between layers, and a tensile stress of 20 MPa. The Mo/Cu multilayer is etched in a 2:1:2 HNO_3:HF:H_2O solution, which is cooled to reduce the etching speed. TES areas vary between 300 μm × 300 μm and 800 μm × 800 μm, and there is little variation in TES performance over areas of several square inches. A 250 nm Mo wiring layer, which also contains the bonding pads, is deposited last by lift-off. Currently, the 250 μm thick Sn foil absorbers, ranging in size between 1 mm × 1 mm and 2 mm × 2 mm, are cut individually and attached by hand using two-component Stycast 2850FT epoxy, loaded with Al_2O_3 grains to match the thermal expansion with that of Cu. Two 25 μm Al wires serve as spacers to ensure that the epoxy has a uniform thickness and that the Sn absorbers do not touch the SiN membrane and provide an alternative path for the heat flow. Full-wafer processes for absorber attachment large detector arrays are currently being developed.

3.2. Spectrometer design

For user-friendly Gamma-ray analysis with TES microcalorimeters we have built a cryogenic spectrometer that holds the detector at the end of a cold finger within ~2 cm of a room temperature radioactive sample (figure 9). The spectrometer uses a nested design, with liquid nitrogen and liquid helium tanks for pre-cooling to 77 K and 4.2 K, respectively [20], and a two-stage adiabatic demagnetization refrigerator (ADR) to attain a base temperature of ~60 mK. Adiabatic demagnetization is a process of cooling below a liquid He bath temperature through isothermal magnetization and adiabatic demagnetization of a paramagnetic material. The process involves lowering a paramagnet's entropy by aligning its spins a magnetic field, while carrying the heat of magnetization into the liquid He bath through a closed heat switch. After opening the heat switch, the magnetic field is decreased sufficiently slowly to keep the entropy of the paramagnet constant, thereby lowering its temperature. Our spectrometer uses two different paramagnets on two separate stages to allow operation with an un-pumped liquid He bath at a temperature of 4.2 K [21, 11]. The first (guard) stage is cooled by a gadolinium gallium garnet $Gd_3Ga_5O_{12}$ (GGG) to a temperature of ~1 K, and the second (detector) stage is cooled to a base temperature of ~60 mK by a $Fe(NH_4)(SO_4)_2 \times 12\ H_20$ salt pill, commonly know as FAA for ferric ammonium alum. The adiabatic demagnetization cycle is automated, takes about ~1 h, and allows detector operation for ~8 to ~20 h between cycles, depending on the heat load into the cold stage and the operating temperature of the detector. During operation, the detector stage temperature can be kept stable to ±10 μK. The TES detector is mounted on the 0.1 K stage at the end of a Au-plated oxygen-free high-conductivity Cu cold finger, which is surrounded by a liquid-He-cooled and a liquid-N_2-cooled radiation shield, and by μ-metal magnetic shielding at room temperature (cf. figure 11). ADRs are compact, reliable and easy to use.

3.3. Single pixel performance

The Mo/Cu TES microcalorimeter with a 1.5 mm × 1.5 mm Sn absorber is cooled down in the ADR, and the ADR bath temperature is regulated to 100 ± 0.01 mK. The TES is voltage biased at the midpoint of the transition, and irradiated with a mixed isotope uranium reference source whose isotope ratio equals that of natural uranium (0.72% ^{235}U, 99.28% ^{238}U). The detector performance does not change significantly with detector bias along the transition, since the noise is dominated by phonon noise $4kT^2G_{abs}$ between the Sn absorber and the TES, and variations in spectrometer sensitivity $\partial R_{TES}/\partial T$ along the superconducting-to-normal transition thus affect signal and noise equally. Figure 10 shows the 92 keV region of the Gamma-spectrum for a 20,000 s exposure. The detector resolution is 90 eV FWHM for

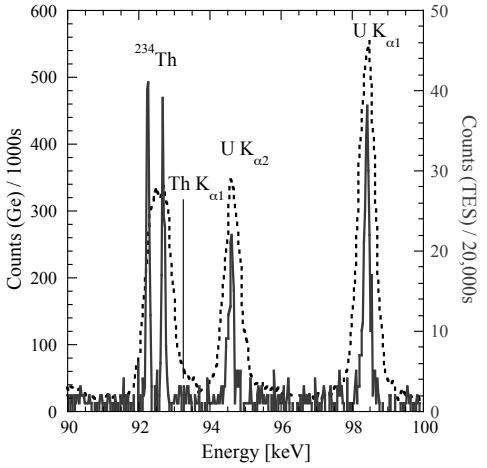

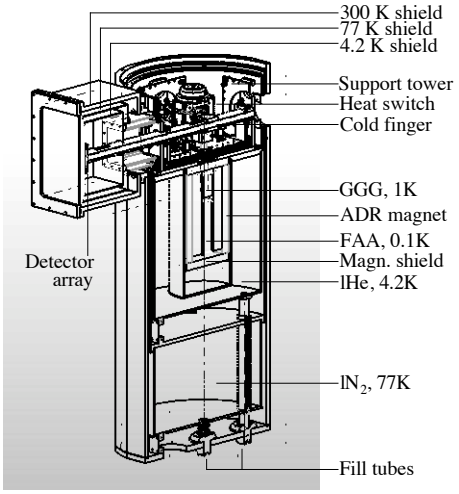

Fig. 9. (left) Cryogenic Gamma spectrometer and support electronics. Gamma rays from the radioactive source on the left and are absorbed by the TES microcalorimeter, which is held at ~0.1 K at the end of the cold finger ~2 cm behind the entrance window. Fig. 10. (center) The 92 keV region in the gamma spectrum of a natural uranium sample, once observed with a Ge detector (dotted) and once with a cryogenic TES microcalorimeter (solid line). Fig. 11. (right) Design of the next-generation Gamma spectrometer with a large cold finger for large-area Gamma-ray detector operation. The cryostat is shown upside down as oriented during assembly.

the two ^{234}Th Gamma-ray lines at 92.38 and 92.80 keV, i.e. the spectrometer has a resolving power of ~1000 at that energy. At this resolution, the difference in natural line width between the ^{234}Th nuclear transitions and the U$K_{\alpha1}$ and U $K_{\alpha2}$ electronic X-ray transitions, whose natural line width of ~90 eV adds to the observed width in quadrature, is clearly visible. For comparison, figure 10 includes a spectrum of the same source taken with a planar HPGe detector during a 2000 s exposure. The trade-off between energy resolution and detection efficiency is obvious. Increasing efficiency of cryogenic detectors and thus spectrometer sensitivity provides the main motivation for building large detector arrays. Arrays will also increase the total count rate capability of the cryogenic spectrometer by a factor equal to the number of independent pixels. This is important, as the intrinsically slow pulse decay time of ~1 ms for these types of composite calorimeters limits the maximum count rate to tens of counts per second per pixel.

This demonstration experiment is an illustrative example for the need for high energy-resolution for non-destructive evaluation of isotope ratios. In principle, the intensity of any two characteristic emission lines can be used for determining the relative abundance of two isotopes in a sample, if their relative radiative yields are known. In practice, lines with similar energies are always preferred, because their use minimizes systematic errors due to the energy dependence of self-absorption inside the sample, shielding transmission and detector efficiency. Lines with similar energy are preferred for high precision measurements even if Ge detectors cannot fully separate them. The 100 keV region of Pu and the 92 keV region of U are two prime examples, and modern analysis routines such as the multi-group analysis programs (MGA) make use of that fact [22, 23].

Precision measurements of uranium enrichment, for example, use the ^{234}Th lines at 92.38 and 92.80 keV as a measure of the ^{238}U abundance, and the Th $K_{\alpha1}$ X-ray at 93.35 keV as a measure of the ^{235}U abundance. This analysis relies on the fact that the strong 186 keV Gamma emission from ^{235}U excites X-rays from the Th daughter of U much more efficiently than radiation released in the decay of ^{238}U. These are by no means the strongest lines in a uranium spectrum, and they only provide an accurate measure of enrichment in samples at least ~120 days old because they require an equilibrium between the ^{234}Th daughter ($\tau_{1/2}$ = 24 days) and the ^{238}U parent, but they are still preferred for analysis because of their spectral proximity [23]. In addition, the 92 keV region is interesting because the U$K_{\alpha1}$ and U $K_{\alpha2}$ electronic X-ray transitions provide a measure of the overall uranium concentration, since the Alpha and Gamma-rays from the uranium decay are more likely to produce U X-rays in the presence of other U atoms near the location of the decay. Furthermore, the relative fluorescence yield of the U $K_{\alpha1}$ and U $K_{\alpha2}$ lines is well known, so that a measurement of their relative spectral intensity provides a local calibration of the efficiency variations with energy. It is

striking that a spectral analysis of the 92 keV region of uranium is still the most precise non-destructive procedure to measure its isotope ratio and thus its degree of enrichment, despite the overlap of the Th $K_{\alpha 1}$ X-ray line at 93.35 keV and the ^{234}Th Gamma emission at 92.80 keV. The advent of large area cryogenic spectrometers that can fully separate the two lines will further enhance this precision significantly.

4. LARGE ARRAY SPECTROMETER DESIGN

4.1. Detector array fabrication

The extension of the detector fabrication to large microcalorimeter arrays is comparably straightforward. Our photolithographic process produces hundreds of TES detectors with very similar characteristics on a 4" wafer. Small residual variations in detector characteristics, mostly in the form of slightly different critical temperatures T_c, are compensated by the self-regulating mechanisms of electrothermal feedback (ETF) [13]. Variations in sensitivities $\partial R_{TES}/\partial T$ have surprisingly little effect on the pulse shape, since ETF only acts on the TES and the pulse shape is set by the absorber heat capacity and the thermal conductance G_{abs} (cf. figure 6). We do not expect the response of each pixel in the array to be identical, and will calibrate each pixel individually. The layout of a 10-channel test array currently under development is shown in figure 12. Individual TES sizes are 500 μm × 500 μm and 800 μm × 800 μm, the larger thermistors allowing larger patches of epoxy to attach the absorber for increased thermal conductivity G_{abs} and reduced noise (cf. figure 8). The 2.5 mm pitch of the pixels allows fine tuning the absorber size for a given application, which will be different for different absorber materials. The large overhang of typical ~2 mm × 2 mm absorbers over the TES pixels simplifies the fabrication of close-packed arrays, since the wiring can be routed conveniently beneath them. The 2.5 mm pixel pitch also ensures that there is enough Si left between the pixels to keep the array mechanically stable and to reduce cross-talk between neighboring pixels. A thick Cu ground plane between pixels serves as an additional phonon sink and further suppresses cross-talk. The wiring connects to the bias circuitry on one side of the array, and to the SQUID readout on the other side. This array layout can be easily extended to 10 × 10 or even larger arrays with current photolithography.

Attaching absorbers in large microcalorimeter arrays is somewhat more involved. For current 10-pixel arrays, and possibly even for 10 × 10 arrays, absorbers can continue to be individually attached by hand. Larger arrays, however, require an automated process for parallel attachment, similar to bump-bonding. This in turn necessitates fabricating the SiN membrane as the last step, since it would otherwise break when pressing the absorbers onto the TES calorimeters. We have already developed a process to cut large sheets of thick absorber metal foils into regular arrays, and we are currently changing our photolithographic process to etch the Si last, i.e. after attaching the absorber arrays.

4.2. Adiabatic demagnetization refrigerator upgrade

The next-generation ADR refrigerator requires mostly an increase in cold finger size to accommodate the detector arrays. In addition, several SQUID preamplifiers must be placed on the 4.2 K stage, preferably close to the main amplifier at room temperature to keep the wiring between 4.2 K and 300 K short and not restrict the amplifier bandwidth. The design of such an ADR is shown in figure 11, which is conceptually identical to our current design. The upgrade features a 4" × 4" detector platform at 0.1 K at the end of the cold finger, and a rack of slots for multiple SQUID preamplifier boards with standardized connectors for multi-wire harnesses to room temperature.

4.3. Multiplexing readout

The challenge for large cryogenic detector arrays lies in the readout of many pixels without increasing the heat load into the cold stage due to the number of wires required. Two approaches are currently being pursued for a multiplexed readout of several detectors with a single SQUID preamplifier. One is time division multiplexing, where a first-stage SQUID multiplexer sequentially samples several detectors [24, 25]. The other is frequency domain multiplexing, where each detector forms the resistive part in an LCR_{TES} resonance circuit and is ac biased at an identifying carrier frequency ω_i. Photon absorption changes the TES resistance, which in turn causes an amplitude modulation of the carrier frequency (figure 13) [26, 27]. This is the approach we are pursuing. The carrier frequencies are spaced sufficiently far to separate the signal from neighboring pixels in the sidebands about the carrier, about 30 kHz for our TES Gamma-ray detectors. We have already shown that two Gamma detector pixels can be multiplexed without degrading the energy resolution of ~60 eV at 60 keV compared to the dc-biased case [10].

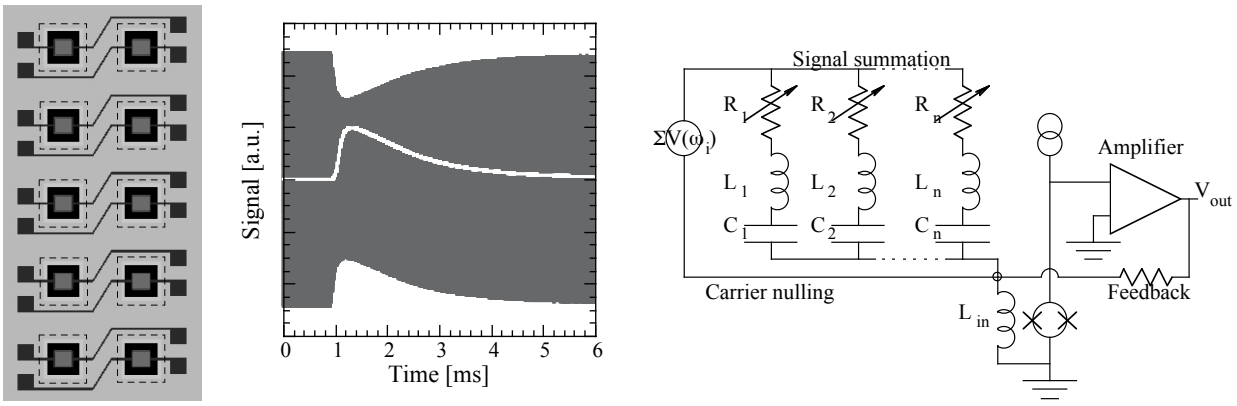

Fig. 12. (left) Mask layout of a 10-channel array of TES microcalorimeters. The pitch of the pixels is 2.5 mm, the central 500 mm × 500 µm TES is placed on a 1 mm × 1 mm membrane (black), and the ~2 mm bulk absorbers (dashed) extend over the wiring layers. This layout allows a straightforward extension to large close-packed arrays. Fig. 13. (center) ac biased microcalorimeter readout (gray) and demodulated waveform (white). The absorption of a Gamma-ray and the subsequent change in TES resistance causes an amplitude modulation of the ac carrier, similar to AM radio. Fig. 14. (right) Circuit diagram for the frequency-multiplexed readout of detector arrays.

Figure 14 shows the implementation of such a frequency-based multiplexing readout for our Gamma spectrometers [28]. Each TES forms part of a LCR tank circuit with a characteristic resonance frequency $\omega_i = 1/\sqrt{(L_i C_i)}$. The inductors and capacitors are selected for a carrier spacing of 30 kHz, and for a sharp resonance set by $Q \equiv \omega_i/\Delta\omega_i = R_i\sqrt{(C_i/L_i)} \approx 1000$. A voltage "comb" consisting of a sum of different sinusoidal carrier frequencies $\Sigma V(\omega_i)$ can be applied to the array over a single connection, with each resonance circuit acting as a sharp filter that selects only the resonant carrier. As in the case of the dc bias circuit, the voltage bias is implemented through a shunt resistor $R_S << R_{TES}$ (not shown in figure 14). The amplitude modulated signals are summed into a single node at the input of the SQUID. The effective finite impedance to ground at that node $|\omega L_{in}|$ contributes the level of crosstalk between neighboring pixels. The feedback signal of the SQUID output is therefore added to the same node to reduce that impedance by the loop gain of the SQUID and the room temperature amplifier. A phase-shifted copy of the carrier signal (phase shifter not shown in figure 14) is added to the same summing loop to null out the carrier signals and thereby reduce the flux burden into the SQUID. A single SQUID can then the used to read out multiple Gamma detector pixels. The maximum number of pixels per SQUID is determined by the ratio of carrier spacing (~30 kHz) to SQUID bandwidth (~1MHz), which in turn is set by phase delay along the cable between the SQUID at 4.2 K and the room temperature electronics. Cables are therefore kept short, around ~20 cm. We expect to be able to multiplex at least ~15, possibly up to ~30 Gamma-ray detector pixels with a single SQUID pre-amplifier. The read-out of larger arrays is possible using multiple parallel SQUIDs.

5. SUMMARY

We have built a cryogenic ultra-high resolution gamma-ray spectrometer based on Mo/Cu multilayer transition-edge sensor (TES) microcalorimeters with attached bulk Sn absorbers. We have also built several two-stage adiabatic demagnetization refrigerators with a cold finger for user-friendly detector operation at ~0.1 K. These spectrometers have achieved an energy resolution between 60 and 90 eV FWHM for Gamma-ray energies up to 100 keV, about a factor of 5 better than the Fano limit of conventional high-purity Ge spectrometers. Two of these detectors can be multiplexed without loss in energy resolution. We are currently working on increasing the spectrometer sensitivity by building large arrays of cryogenic Gamma-ray microcalorimeter detectors and their multiplexed readout. This will greatly enhance the precision of isotope ratio measurements for nuclear forensics and nuclear non-proliferation applications, particularly for the attribution of unknown materials based on isotopic fingerprinting.

ACKNOWLEDGEMENTS

We gratefully acknowledge the financial support of the U.S. Department of Energy, Office of Non-Proliferation Research and Engineering, NA-22. This work was performed under the auspices of the U.S. Department of Energy by University of California Lawrence Livermore National Laboratory under contract No. W-7405-Eng-48.

REFERENCES

1. For a recent overview of the filed of cryogenic detectors, see the *Proceedings of the 10th International Workshop on Low Temperature Detectors*, LTD-10, edited by F. Gatti, published as *Nucl. Inst. Meth*. **A 520** (2004)
2. S.H. Moseley, J.C. Mather, D. McCammon, *J. Appl. Phys*. **56** (5), 1257-1262 (1984)
3. D. McCammon et al., *Astrophysical Journal* **576** (1), 188-203 (2002)
4. A. Bleile, P. Egelhof, H.J. Kluge, U. Liebisch, D. McCammon, H.J. Meier, O. Sebastian, C. K Stahle, M. Weber. *Nucl. Inst. Meth.* **A 444** (1-2), 488-491 (2000)
5. E. Silver, H. Schnopper, S. Bandler, N. Brickhouse, S. Murray, M. Barbera, E. Takacs, J.D. Gillaspy, J.V. Porto, I. Kink, J.M. Laming, N. Madden, D. Landis, J. Beeman, E.E. Haller, *Astrophysical Journal* **541** (1), 495-500 (2000)
6. E. Silver et al., *SPIE Proceedings* **4851**, 905-912 (2003)
7. C. Enss, *AIP Conference Proceedings* **605**, 5-10 (2002)
8. D.T. Chow, M.A. Lindeman, M.F. Cunningham, M. Frank, T.W. Barbee Jr, S.E. Labov, *Nucl. Inst. Meth.* **A 444** (1-2), 196-200 (2000)
9. D.T. Chow, M.L. van den Berg, A. Loshak, M. Frank, T. W. Barbee Jr, S.E. Labov SE, *IEEE Trans. Appl. Superconductivity* **11** (1), 743-746 (2001)
10. M.F. Cunningham, J.N. Ullom, T. Miyazaki, S.E. Labov, J. Clarke, T.M Lanting, A. T. Lee, P.L. Richards, J. Yoon, H. Spieler, *Appl. Phys. Lett.* **81** (1), 159-161 (2002)
11. S. Friedrich, T. Niedermayr, O. Drury, M.F. Cunningham, M.L. van den Berg, J.N. Ullom, A. Loshak, T. Funk, S.P. Cramer, J.D. Batteux, E. See, M. Frank, S.E. Labov, *Nucl. Inst. Meth.* **A 467**, 1117-1120 (2001)
12. K.D. Irwin, G. C. Hilton, D.A. Wollman, J.M. Martinis, *J. Appl. Phys*. **83** (3), 3978-3985 (1998)
13. K.D. Irwin, *Appl. Phys. Lett*. **66** (15), 1998-2000 (1995)
14. K.D. Irwin, G.C. Hilton, J.M. Martinis, S. Deiker, N. Bergren, S.W. Nam, D.A. Rudman, D.A. Wollman, *Nucl. Inst. Meth*. **A 444** (1-2), 184-187 (2000)
15. W.M. Bergmann Tiest, H.F.C. Hoevers, W.A. Mels, M.L. Ridder, M.P. Bruijn, P.A.J. de Korte, M.E. Huber, *AIP Conference Proceedings* **605**, 199-202 (2002)
16. M.A. Lindeman, R.P. Brekosky, E. Figueroa-Feliciano, F.M. Finkbeiner, M.Li, C.K. Stahle, C.M. Stahle, N. Tralshawala, *AIP Conference Proceedings* **605**, 203-206 (2002)
17. S. Terracol, T. Miyazaki, U. Morita, Y. Ishisaki, K. Tanaka, K. Mitsuda, S. Friedrich, *Nucl. Inst. Meth*. **520** , 300-302 (2004)
18. A. Alessandrello et al., *IEEE Trans. Nucl. Sci.* **40**, 649 (1993)
19. T. Miyazaki et al., in preparation
20. Infrared Laboratories Inc., Tucson, AZ, USA; http://www.irlabs.com/
21. C. Hagmann, P.L. Richards, *Cryogenics* **34**, 221 (1994)
22. R. Gunnink, UCRL-LR-103220, volume 1 (ISPO No. 317, task No. A161), available from the National Technical Information Service, U.S. Dept. of Commerce, 5285 Port Royal Rd., Springfield, VA 22161
23. D. Reilly, N Ensslin, H. Smith Jr., S. Kreiner, "Passive Non-Destructive Assay of Nuclear Materials", Office of Nuclear Regulatory Research, (NUREG/ CR-5550), Washington (1991)
24. K.D. Irwin, *Physica C* **368** (1-4), 203-210 (2002)
25. J.A. Chervanek, K.D. Irwin, E.N. Grossman, J.M. Martinis, C.D. Reintsema, M.E. Huber, *Appl. Phys. Lett.* **74** (26), 4043-4045 (1999)
26. J. Yoon, J. Clarke, J.M. Gildemeister, A.T. Lee, M. J. Myers, P.L. Richards, J.T. Skidmore, *Appl. Phys. Lett*. **78**, 371-373 (2001)
27. T.M. Lanting, H.M. Cho, J. Clarke, M. Dobbs, A.T. Lee, M. Lueker, P.L. Richards, A.D. Smith, H.G. Spieler, *Nucl. Inst. Meth*. **520**, 548-550 (2004)